



# Graphene oxide and carbon nitride nanosheets co-modified silver chromate nanoparticles with enhanced visible-light photoactivity and anti-photocorrosion properties towards multiple refractory pollutants degradation

Fei Chen<sup>a,b</sup>, Qi Yang<sup>a,b,\*</sup>, Shana Wang<sup>a,b</sup>, Fubing Yao<sup>a,b</sup>, Jian Sun<sup>a,b</sup>, Yali Wang<sup>a,b</sup>,  
Chen Zhang<sup>a,b</sup>, Xiaoming Li<sup>a,b</sup>, Chenggang Niu<sup>a,b</sup>, Dongbo Wang<sup>a,b,\*</sup>, Guangming Zeng<sup>a,b</sup>

<sup>a</sup> College of Environmental Science and Engineering, Hunan University, Changsha 410082, PR China

<sup>b</sup> Key Laboratory of Environmental Biology and Pollution Control (Hunan University), Ministry of Education, Changsha 410082, PR China

## ARTICLE INFO

### Article history:

Received 19 January 2017

Received in revised form 22 February 2017

Accepted 5 March 2017

Available online 6 March 2017

### Keywords:

Photocatalysis

Anti-photocorrosion

GO/ACR/CN

Synergistic effect

Double Z-scheme transfer

## ABSTRACT

In this work, a ternary composite photocatalyst consisted of graphitic carbon (g-C<sub>3</sub>N<sub>4</sub>), graphene oxide (GO) and Ag<sub>2</sub>CrO<sub>4</sub> was successfully synthesized through one-step chemical precipitation route. The GO/Ag<sub>2</sub>CrO<sub>4</sub>/g-C<sub>3</sub>N<sub>4</sub> (GO/ACR/CN) nanocomposite exhibited superior photocatalytic performance towards dyes (rhodamine (RhB) and methylene blue (MB)) and two other refractory pollutants (phenol and oxytetracycline) degradation under visible light irradiation. The efficient photo-induced electron-hole pairs separation, multi-step charge transfer and enhanced visible light absorption should be concluded as the synergistic effects among three components, resulting in the improved photoactivity. The decreased degradation efficiency of RhB (MB) over bare ACR was about 25.74% (43.22%) after four times cycles, while insignificant loss was perceived over GO/ACR/CN. The corresponding anti-photocorrosion property was further confirmed by X-ray diffraction (XRD), X-ray photoelectron spectroscopy (XPS) and Fourier transform infrared spectroscopy (FTIR). For in-depth insight into practical applications, the effects of initial concentration and different water sources were also taken into discussions. This work demonstrated that rational and design of ternary nanocomposites could provide a new approach for the development of more efficient visible-light photocatalysts for wastewater treatment and environmental remediation.

© 2017 Elsevier B.V. All rights reserved.

## 1. Introduction

Over the past decades, the increasing industrialization has brought out massive products of dyes, phenols, pesticides, antibiotics, solvents and other refractory organic contaminants with potentially carcinogenic intermediates in natural water resources [1–5]. In order to resolve the more and more serious water pollution crisis, semiconductor-based photocatalysis has attracted considerable attention as a potential and environment-friendly solution to decompose pollutants with high toxicity in wastewater by the utilization of solar light energy [6–10]. Among numer-

ous semiconductor photocatalysts, graphitic carbon (g-C<sub>3</sub>N<sub>4</sub>, CN) has been regarded as a promising photocatalyst for wastewater treatment because of its simple synthesis, superior photocatalytic performance, preferable photochemical stability and low toxicity [11–13]. However, there are still some drawbacks that restricted the applications of CN in environmental remediation, for example, the relatively wide bandgap (about 2.75 eV), low surface area of bulk CN, poor quantum yield and high recombination rate of photo-generated electron-hole pairs [14,15]. So appropriate modifications should be adopted to widen its visible light region absorption, enlarge surface area as well as charge transfer rate and separation efficiency. Up to now, continuous attempts have been devoted to improve the photocatalytic efficiency of bare CN, including doping metals or nonmetals [16,17], regulating shape [18,19] and constructing heterostructured photocatalysts between CN and another semiconductor with suitable band potential [20].

\* Corresponding authors at: College of Environmental Science and Engineering, Hunan University, Changsha 410082, PR China.

E-mail addresses: [feichen@hnu.edu.cn](mailto:feichen@hnu.edu.cn) (F. Chen), [feichen@hnu.edu.cn](mailto:feichen@hnu.edu.cn), [yangqi@hnu.edu.cn](mailto:yangqi@hnu.edu.cn) (Q. Yang).

Researches demonstrated that the construction of heterojunction photocatalyst is more effective since the photo-generated electron-hole pairs were effectively transferred and separated. As a result, strenuous efforts had been made to design CN-based binary heterojunctions, like CN/BiVO<sub>4</sub> [21], CN/BiOBr [22], CN/Ag<sub>3</sub>PO<sub>4</sub> [11,13], CN/TiO<sub>2</sub> [23], CN/ACR [24,25], CN/SmVO<sub>4</sub> [26] and so on. In these binary systems, the recombination rate of photo-induced electron-hole pairs was significantly inhibited and the charge separation efficiency was also increased, so the corresponding visible light photoactivity was enhanced. In our work, Ag<sub>2</sub>CrO<sub>4</sub> (ACR) was adopted to improve CN photoactivity, due to its strong visible light absorption (~720 nm [25]). The more negative conduction band of CN (−1.24 eV) was also beneficial to achieve stronger reducing characteristics and produce more active species. Recently, researches proved that layer CN nanosheets with higher specific surface area exhibited many intriguing properties, which are different from bulk CN [16]. Therefore, CN nanosheets were prepared in our work to provide greater reaction area and shorter photogenerated carrier diffusion length for reducing their photo-generated electron-hole pairs recombination efficiency and promoting higher pollutants removal rate.

However, the photocatalytic activity of these binary systems is still not sufficient in practical activity since the limited region of visible light response and relatively lower photo-induced electron-hole pairs separation efficiency [27,28]. In order to further promote the charge separation and transfer characteristics, ternary system construction was developed and confirmed as an effective method, which could lead to multistep charge transfer and remarkable enhancement of photocatalytic activity. For example, Wei and his co-workers designed TiO<sub>2</sub>/rGO/Cu<sub>2</sub>O ternary heterostructure to achieve more photoelectrochemical hydrogen production, and the synergistic effect of TiO<sub>2</sub>, rGO and Cu<sub>2</sub>O improved the absorption spectrum range and electron/hole separation, resulting in enhanced photocurrent intensity and incident photon-to-photocurrent efficiency [29]. Zhang et al. successfully introduced ZnO into CdS/TiO<sub>2</sub> system to construct ZnO/CdS/TiO<sub>2</sub> hybrid for refractory pollutants degradation and the anti-photocorrosion capacity of CdS was greatly strengthened because the outer ZnO acted as a solid sacrificial reagent in ternary ZnO/CdS/TiO<sub>2</sub> system [30]. According to previous studies [29], graphene oxide (GO) or reduced graphene oxide (rGO) has been identified as one of the most ideal supports for charge carriers separation and transfer for its large specific surface area, high stability and excellent charge carriers mobility. Considering above-mentioned advantages, CN and GO/rGO were simultaneously added into single semiconductor to fabricate novel ternary heterojunction photocatalysts, successful cases such as rGO/Bi<sub>2</sub>WO<sub>6</sub>/CN [31], rGO/ZnS/CN [28], rGO/TiO<sub>2</sub>/CN [32], rGO/(C<sub>16</sub>H<sub>33</sub>(CH<sub>3</sub>)<sub>3</sub>N)<sub>4</sub>W<sub>10</sub>O<sub>32</sub>/CN [33] and GO/Ag<sub>3</sub>PO<sub>4</sub>/CN [34]. Similarly, common problems of binary nanocomposites might exist in CN/ACR heterojunctions, thus it seemed to be feasible for assembling GO/ACR/CN ternary photocatalyst with enhanced photocatalytic activity and stability. To our knowledge, this type of ternary photocatalyst has not been reported yet.

Herein, GO/ACR/CN nanocomposite was fabricated by a facile precipitation route and employed in multiple pollutants degradation under visible light irradiation. Compared with ACR, CN, ACR/GO and ACR/CN, GO/ACR/CN ternary photocatalyst displayed the obviously enhanced photocatalytic performance. The improved photoactivity should attribute to the synergistic effect between ACR, CN and GO, including effective photo-induced electron-hole pairs separation, multistep charge transfer, enhanced surface area and visible light adsorption. The combination of ACR nanoparticles with GO and CN sheets might also effectively prevent the dissolution of ACR and thus improved its photostability, which could be confirmed by XRD, XPS and FTIR tests. The predominant active species were investigated by radicals trapping experiments and ESR

measurements. A possible double Z-scheme degradation mechanism was also proposed. This work sheds light on a new kind of ternary photocatalysts with higher stability and visible light photocatalytic performance for organic pollutants decomposition, containing of one semiconductor, CN and GO/rGO.

## 2. Experimental section

### 2.1. Photocatalysts preparation

All chemicals were of analytical grade and without further purification before use. De-ionized water was employed throughout all experiments. The GO and CN nanosheets were prepared as our previous reports [8,27]. The GO/ACR/CN ternary composites were fabricated by a facile chemical precipitation method. Briefly, the prepared GO (0.010 g) and CN (0.300 g) nanosheets were separately dispersed in 50 mL de-ionized water by ultrasonication for 1 h. Simultaneously, AgNO<sub>3</sub> (0.307 g) and K<sub>2</sub>CrO<sub>4</sub> (0.175 g) were dissolved in two 20 mL de-ionized water, respectively. The forming AgNO<sub>3</sub> and K<sub>2</sub>CrO<sub>4</sub> solutions were dripped into GO and CN suspension, respectively. After that, these mixtures were constantly stirred for 12 h under room temperature, so that Ag<sup>+</sup> and CrO<sub>4</sub><sup>2−</sup> ions would be well adsorbed or dispersed on the surface of GO and CN, respectively. Then the obtained homogeneous suspension containing CN and K<sub>2</sub>CrO<sub>4</sub> was added dropwise into GO mixture. After another 4 h stirring, the GO/ACR/CN ternary composites were collected by filtration, washed with ethanol and de-ionized water for several times and finally dried at 60 °C in an oven for 12 h. For comparison, ACR/GO and ACR/CN were also synthesized in the same way as the composite of GO/ACR/CN with the absence of CN and GO, respectively.

### 2.2. Characterization

X-ray diffraction (XRD) patterns were collected using a Rigaku D/max 2500 v/pc X-ray diffractometer with Cu K $\alpha$  irradiation. The morphologies investigation was performed by a field emission scanning electron microscope (FESEM, Hitachi S-4800) and a transmission electron microscope (TEM, FEI Tecnai G20). The X-ray photoelectron spectroscopy (XPS) was analyzed on a Thermo ESCALAB 250XI spectrometer with Al K $\alpha$  source. Fourier transform infrared spectroscopy (FTIR) was measured on an IR Prestige-21 spectrometer (Shimadzu, Japan) with scan range from 400 to 4000 cm<sup>−1</sup> after pressing into tablets with KBr powder. Ultraviolet-visible (UV-vis) diffuse reflectance spectra were measured by the spectrophotometer (UV-4100, Shimadzu) with BaSO<sub>4</sub> as reference. The total organic carbon (TOC) assays were tested using a Shimadzu TOC-VCPH analyzer. The Photoluminescence (PL) spectroscopy was obtained using a transient fluorescence spectrometer (Edinburgh FLsp920). The special surface area was detected by Brunauer-Emmett-Teller (BET) technology from the N<sub>2</sub> adsorption isotherm, which was evaluated at 77 K on a TRISTAR-3000 surface area analyzer. The electron spin resonance (ESR) signals were examined on a Bruker ER200-SRC spectrometer under visible light irradiation ( $\lambda > 420$  nm). The electrochemical impedance spectroscopy (EIS) was performed on an electrochemical workstation (CHI660C) in a typical three-electrode system.

### 2.3. Photocatalytic degradation experiments

The photocatalytic activities of the catalysts were investigated through the photodegradation of multiple refractory pollutants irradiated by a 300 W Xe lamp with a 420 nm UV-cutoff filter. In a typical experiment, 0.02 g photocatalyst was added into 100 mL of synthetic wastewater (15 mg/L rhodamine (RhB), 15 mg/L methylene blue (MB), 10 mg/L phenol or 10 mg/L oxytetracycline). Before

exposed to visible light, the suspension was magnetically stirred in dark for 30 min to reach the adsorption-desorption equilibrium. An aliquot (4 mL) was withdrawn at regular intervals with centrifugation to separate solids and measured the residual pollutant concentration by a UV–vis spectrophotometer (RhB, MB) and HPLC (phenol, oxytetracycline) analysis. The degradation efficiency was calculated according to  $\eta = (C_t - C_0)/C_0$ , where  $\eta$  is the degradation efficiency,  $C_t$  and  $C_0$  represent the concentration of reactant at the time of  $t$  and 0, respectively. Moreover, the radicals capture experiments were carried out with similar procedure to above-mentioned photocatalytic reaction, except that 1 mmol ethylenediaminetetraacetic acid disodium (EDTA-2Na, a quencher of  $h^+$ ), 1 mmol isopropanol (IPA, a quencher of  $\cdot OH$ ) and 1 mmol 1,4-benzoquinone (BQ, a quencher of  $\cdot O_2^-$ ) [5], were added respectively.

### 3. Results and discussion

#### 3.1. Characterization of the as-prepared samples

Fig. 1 shows the XRD patterns of the synthesized photocatalysts, which provides more information on their specific crystal structures. The original CN sample displays strong peaks centered at  $2\theta$  values of  $13.0^\circ$  and  $27.6^\circ$ , corresponding to the (100) and (002) planes of the graphite-like structure of CN [20]. The structure of pure ACR nanoparticles was matched well with orthorhombic ACR (JCPDS No. 26-0952 [24]). As detected from Fig. 1, ACR/GO possesses almost the same XRD patterns compared to that of ACR, suggesting the negligible effect graphene oxide poses upon ACR structure. The relatively low quantity of graphene oxide in this composite might be the main reason for the invisible peak of GO [8]. For ACR/CN and GO/ACR/CN nanocomposites, all diffraction peaks belonging to CN and ACR could be found, indicating the successful incorporation of CN in these two samples. Moreover, the characteristic peak at  $13.0^\circ$  indexed to the (100) crystal plane almost disappeared because of low crystallinity of CN, the result agrees with other published reports [15].

The morphologies were of the as-prepared characterized by SEM technology. From Fig. 2A, GO reveals smooth and crumpled sheets resulting from the deformation and distortion of graphite sheets. ACR presented as uniform particles in Fig. 2B. Pure CN dis-

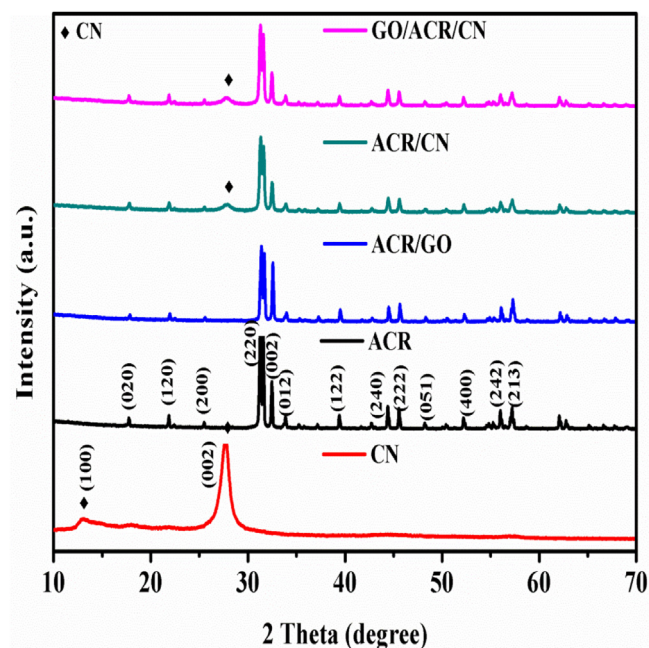


Fig. 1. XRD patterns of the as-prepared samples.

plays wrinkled lamellar structure with relatively smooth surface (Fig. 2C). While ACR particles in the ACR/GO composite were closely enveloped by gauze-like GO sheets (Fig. 2C). As shown in Fig. 2D, ACR particles were loaded on the surface of CN and wrapped with g-C<sub>3</sub>N<sub>4</sub>. For GO/ACR/CN (Fig. 2F), three structures were all found and combined well with each other. The TEM test was adopted to further confirm the results that the catalysts were successfully prepared. The typical TEM images of ACR, CN, ACR/GO, ACR/CN and GO/ACR/CN were exhibited in Fig. 3A–F, respectively. Besides, High-resolution transmission electron microscopy (HRTEM) images were employed to evaluate the effective contact interface of two or more semiconductors. From Fig. 3G–3I, we could clearly find the lattice fringes with the interplanar spacing of 0.274 nm, 0.203 nm, 0.204 nm were observed, corresponding to the (002), (240), (240) planes of ACR in ACR/GO, ACR/CN and

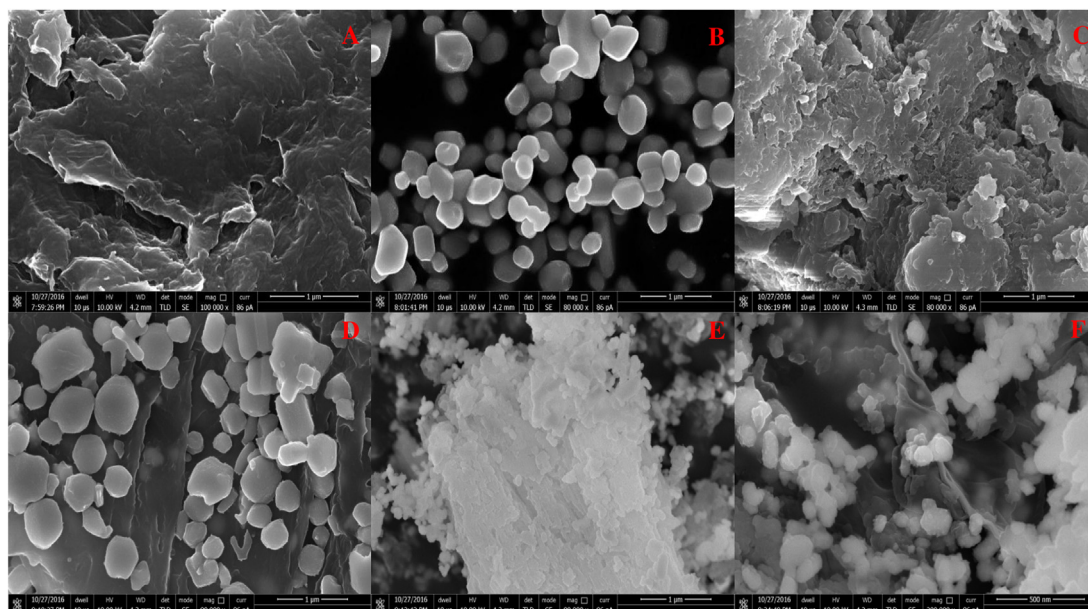
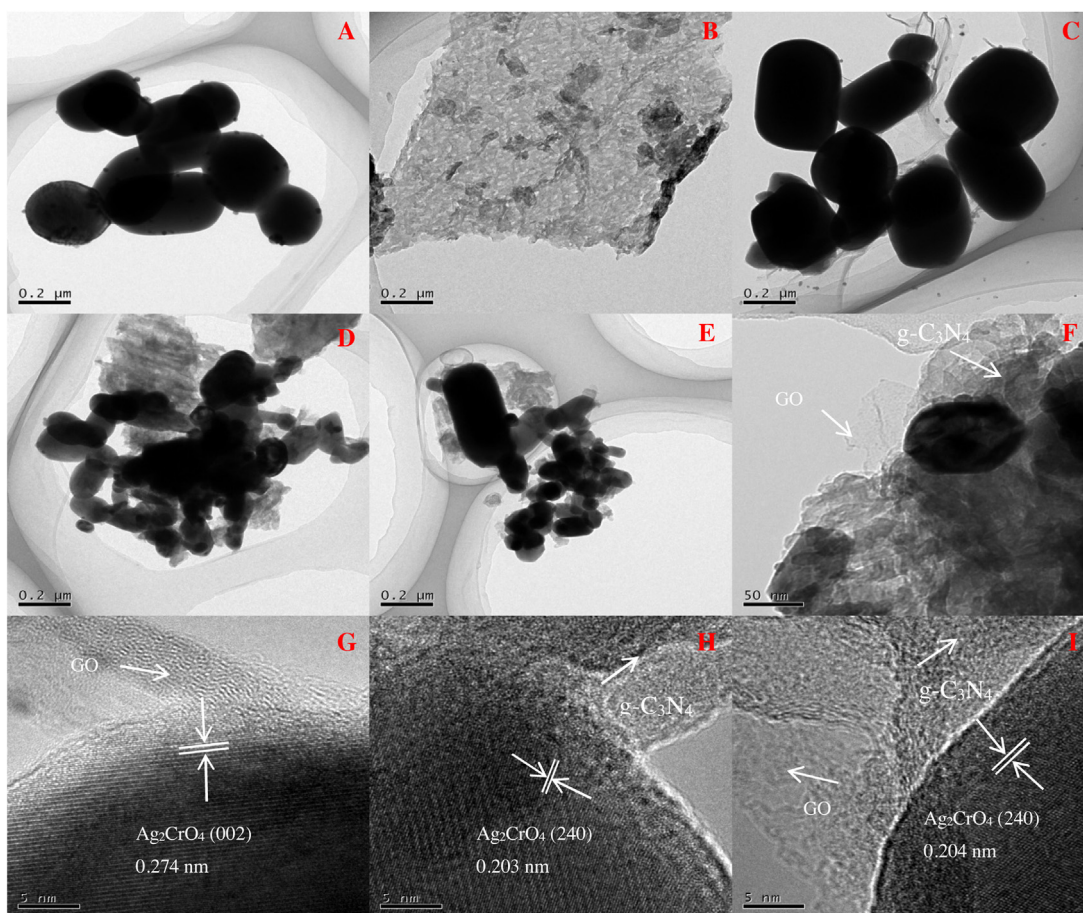


Fig. 2. SEM images of prepared samples: GO (A), ACR (B), CN (C), ACR/GO (D), ACR/CN (E), GO/ACR/CN (F).





**Fig. 3.** TEM images of ACR (A), CN (B), ACR@GO (C), ACR/CN (D), GO/ACR/CN (E–F) and HRTEM images of ACR/GO (G), ACR/CN (H), GO/ACR/CN (I).

GO/ACR/CN nanocomposites, respectively. The GO, CN or GO/CN also exhibited sheet-like morphologies and well attached to ACR nanoparticles, which were marked up in HRTEM images for better visibility.

The surface chemical composition and states of GO/ACR/CN nanocomposite was further examined by XPS. It is obviously seen that only elements of C, N, Ag, Cr and O could be found in the XPS survey spectrum (Fig. 4A) of the nanocomposite, and no impurities are detectable. The high-resolution C 1s XPS spectrum is displayed in Fig. 4B, four typical peaks are located at 283.9 eV, 285.6 eV, 286.9 eV and 287.4 eV, which could be ascribed to the  $sp^2$  bonded carbon (C–C), defect-containing  $sp^2$ -hybridized carbons, epox-/hydroxyls (C–O) and carbonyls (C=O), respectively [35,36]. The high resolution N 1s spectrum of GO/ACR/CN (Fig. 4C) can be separated into four characteristic peaks appearing at 397.8 eV, 398.8 eV, 400.2 eV and 403.8 eV, which could be attributed to the  $sp^2$  hybridized aromatic N bonded to carbon atoms (C=N–C), tertiary nitrogen N–(C)<sub>3</sub> groups, N–H structure and  $\pi$  excitations, respectively [27,32]. Fig. 4D presents the Cr 2p spectrum, two individual peaks with binding energies of 577.9 eV and 587.2 eV could be assigned to Cr 2p<sub>3/2</sub> and Cr 2p<sub>1/2</sub>, respectively. Another peak at 571.9 eV might belong to Ag 3p<sub>3/2</sub> [25]. Two obvious peaks (Fig. 4E) situated at binding energies of 366.9 eV and 372.8 eV corresponded to Ag 3d<sub>5/2</sub> and Ag 3d<sub>3/2</sub>, and they couldn't be divided into four peaks, indicating only the existence of Ag<sup>+</sup> in the fresh GO/ACR/CN nanocomposite. Based on the results of XRD, SEM, TEM, HRTEM and XPS measurements, the close combination among ACR, CN and GO in GO/ACR/CN system had been validated.

The optical property plays an important role in determining the photocatalytic activity of semiconductor photocatalysts. The

UV–vis diffuse reflectance spectra (DRS) of the whole samples were depicted in Fig. 5A. For pure CN, an absorption edge at about 450 nm was presented, whereas a broad adsorption in almost whole visible light region for pure ACR (~720 nm), suggesting that an effective utilization of solar light over ACR was obtained. Obviously, the absorption intensity of ACR/CN was enhanced in visible light region. The drastically strengthened photo-absorption was also observed for ACR/GO composite, which could be ascribed to the fact that graphene oxide could reduce the reflection of light [33]. While for ternary GO/ACR/CN composite, the widest visible light absorption was achieved, indicating that the synergistic effect between ACR, CN and GO worked. That was to say, GO/ACR/CN nanocomposite could efficiently utilize visible light and produce more photo-induced electron-hole pairs under visible light illumination. In addition, the band gap ( $E_g$ ) of ACR and CN could be calculated by following formula (Eq. (1) [37,38]):

$$\alpha h\nu = A(h\nu - E_g)^{n/2} \quad (1)$$

where  $A$ ,  $E_g$ ,  $h$ ,  $\alpha$  and  $\nu$  are proportionality constant, band gap, Planck constant, absorption coefficient and light frequency, respectively. The  $n$  value is determined by the type of optical transition of semiconductors ( $n=1$  for direct transition and  $n=4$  for indirect transition). Both ACR and CN belong to the indirect transition semiconductors (Fig. 5B), and the corresponding  $E_g$  values of ACR and CN from the plots of  $(\alpha h\nu)^2$  versus energy ( $h\nu$ ) were estimated to be about 1.72 eV and 2.75 eV, respectively. Additionally, the conduction band potential ( $E_{CB}$ ) and valence band potential ( $E_{VB}$ ) of

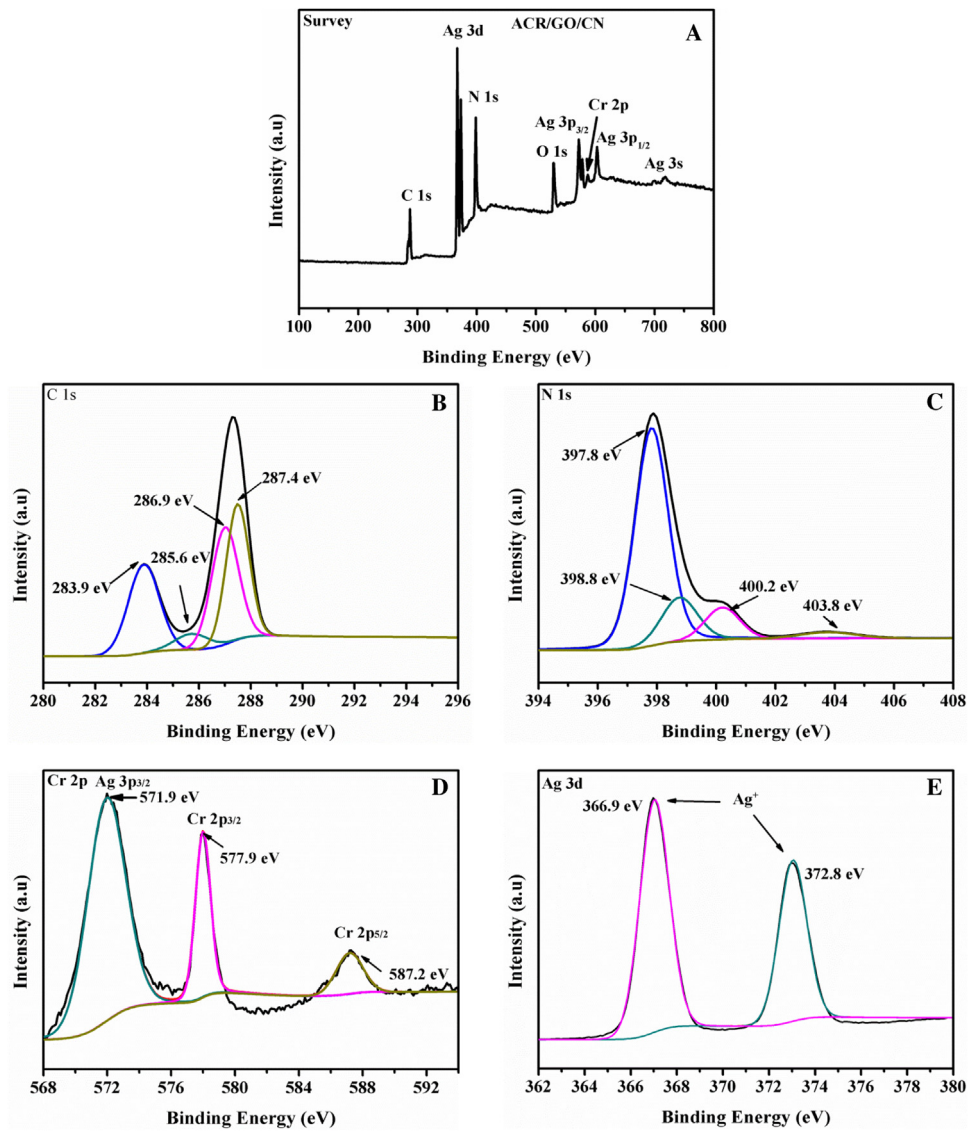


Fig. 4. XPS spectra of GO/ACR/CN: Survey spectrum (A), C 1s (B), N 1s (C), Cr 2p (D) and Ag 3d (E).

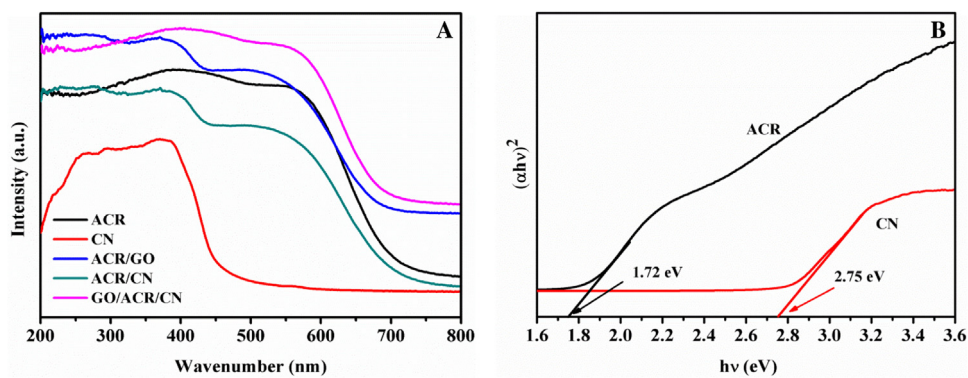


Fig. 5. UV-vis adsorption spectra of prepared samples (A) and calculated band gap of ACR and CN (B).



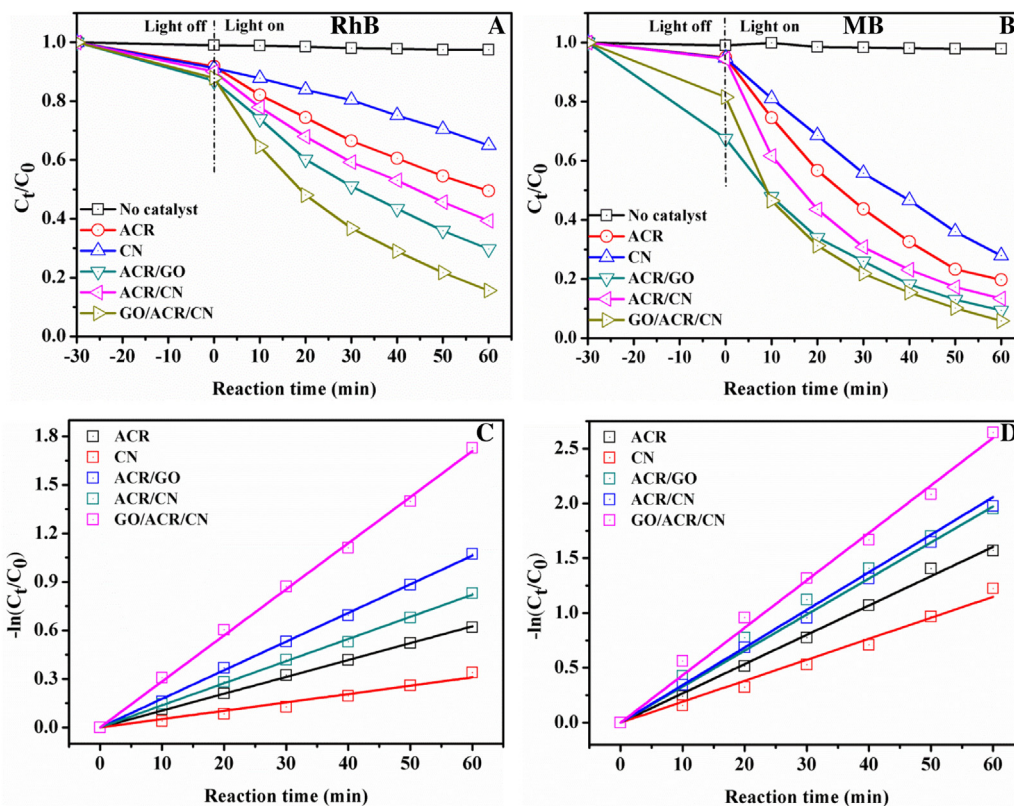


Fig. 6. Photodegradation degradation of RhB (A) and MB (B) under visible light irradiation,  $-\ln(C_t/C_0)$  versus time curves of RhB (C) and MB (D) degradation.

the semiconductors could be calculated by the following empirical equations [39]:

$$E_{CB} = X - E^c - 0.5E_g \quad (2)$$

$$E_{VB} = E_{CB} + E_g \quad (3)$$

where  $X$  is the electronegativity of the semiconductor,  $E^c$  is the energy of free electrons on the hydrogen scale ( $\sim 4.50$  eV vs NHE). Therefore, the  $E_{VB}$  potentials of CN and ACR were +1.51 eV and +2.22 eV, and corresponding  $E_{CB}$  potentials could be estimated to be  $-1.24$  eV and  $+0.50$  eV, respectively.

### 3.2. Visible light photocatalytic activities

The photocatalytic activities were firstly evaluated by the degradation of two single dyes (RhB and MB) in aqueous solution under visible light irradiation at room temperature. Fig. 6A–B showed the photocatalytic degradation efficiencies ( $C_t/C_0$ ) of dyes induced by ACR, CN, ACR-based binary and ternary nanocomposites. In blank test, self-degradation of RhB or MB was negligible without the addition of catalysts, suggesting the relatively photochemical stability of these organic dyes. For pure ACR and CN, dye degradation efficiencies were unsatisfactory, which about 46.16% (79.52%) and 28.76% (70.58%) for RhB (MB), respectively. Compared to single photocatalyst, ACR-based binary and ternary nanocomposites exhibited substantially enhanced photocatalytic performance. Especially, GO/ACR/CN sample achieved the highest degradation efficiencies, where 82.23% of RhB and 92.69% of MB were removed under identical conditions. The better photocatalytic properties should be attributed to the coexisting effects among ACR, GO and CN, resulting in wider visible-light absorption and photo-generated electron-hole pairs separation and efficient pollutant degradation.

It was worth noticing that the photocatalytic decomposition of RhB or MB was supposed to follow a pseudo-first-order kinetics reaction, and the evaluating formula was expressed as Eq. (2) [5]:

$$\ln\left(\frac{C_t}{C_0}\right) = -k_{app}t \quad (4)$$

where  $k_{app}$  is the apparent rate constant ( $\text{min}^{-1}$ ).  $C_0$  and  $C_t$  is the TC concentration at reaction time 0 and  $t$ , respectively. As shown in Fig. 6C–D and Fig. 7A–B, the kinetic constants induced by GO/ACR/CN were estimated to be  $0.02849 \text{ min}^{-1}$  (RhB) or  $0.04329 \text{ min}^{-1}$  (MB), which were 2.73 (5.52) or 1.62 (2.26) times higher than those of ACR and CN, respectively. The relative degradation rates kept the same order:  $\text{CN} < \text{ACR} < \text{ACR/CN} < \text{ACR/GO} < \text{GO/ACR/CN}$ . Meanwhile, contaminant mineralization ability worked as a vital parameter for photocatalytic performance evaluation. Thus, TOC removal efficiencies of the as-prepared samples were also investigated during MB degradation. As depicted in Fig. 8C, the mineralization ratio of pure ACR, ACR/CN, ACR/GO and GO/ACR/CN was 25.32%, 34.23%, 40.51% and 57.45%, indicating that higher mineralization ability was acquired by modified ACR. The GO/ACR/CN ternary nanocomposite exhibited the highest TOC removal efficiency, which ensured its practical application potentials. As a result, GO/ACR/CN ternary nanocomposite could be utilized as an efficient photocatalyst for the degradation of dye pollutants. Further to determine the excellent visible-light photoactivity of GO/ACR/CN, two refractory pollutants (phenol and oxytetracycline) were also chosen as the objective. As shown in Fig. 8D, about 94.21% (81.34%) of phenol (oxytetracycline) was decomposed within 90 min light irradiation. The results suggested the enormous potentiality of GO/ACR/CN for complex organic pollutants removal. As interlayers, graphene oxide harassed the ACR as well as  $g\text{-C}_3\text{N}_4$  insides the samples and participated in electrical conduction and bridged the gap between ACR and CN, facilitating the separation of photoinduced charge and

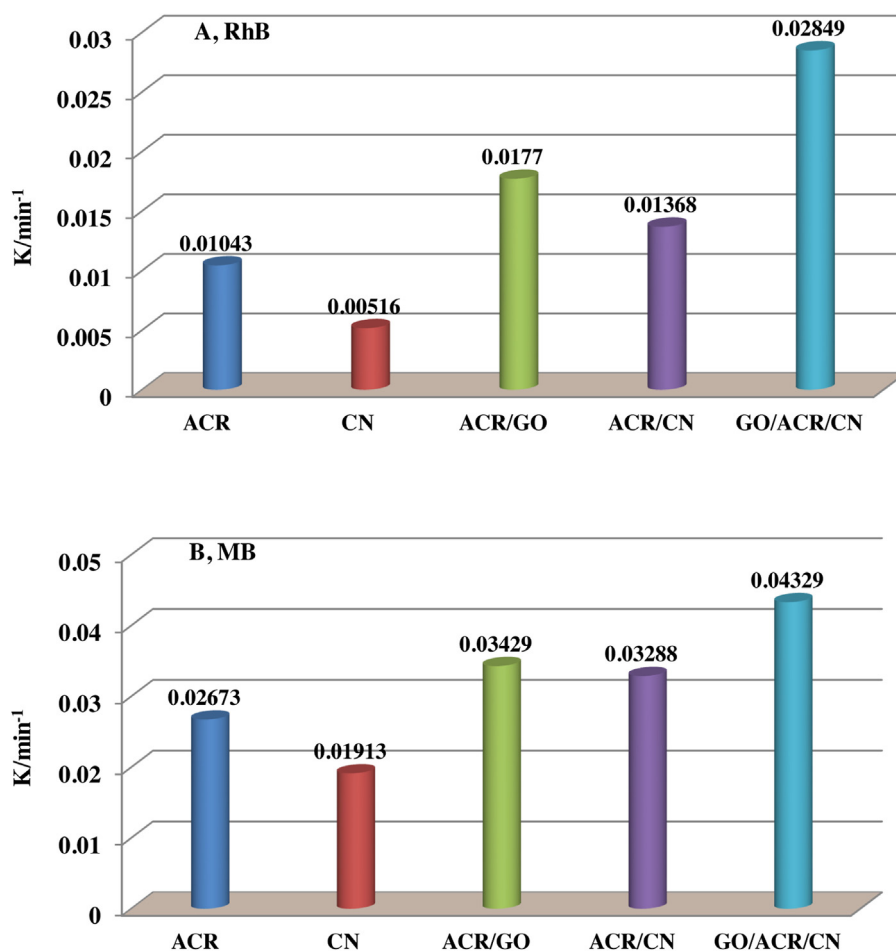


Fig. 7. The apparent rate constants over all samples for the degradation of RhB (A) and MB (B).

reducing the recombination possibility of photoexcited electrons and holes.

In practical wastewater systems, pollutants concentration and coexisting pollutants might be the major factors for dye wastewater removal. Herein, these two parameters also had been taken into discussion. The MB degradation efficiencies (Fig. 8A) declined from 92.69% to 62.86% with the initial dye concentration increasing from 15 mg/L to 50 mg/L. The higher initial dye solution increased the photons pathways entering the dye solution but it also induced the competitive adsorption between dyes and dyes intermediates on catalyst surface. For achieving higher photodegradation efficiency, pre-treatment process was necessary to reduce the initial dye concentration, such as dilution, cyclic treatment. In order to investigate the effect of coexisting pollutants on the degradation of MB over GO/ACR/CN nanocomposite, the photodegradation experiments were carried out using different wastewater sources and the results were displayed in Fig. 8B. The decomposition efficiencies were 92.69%, 78.45%, 82.35% and 86.42% when using de-ionized water, municipal water, river water and tap water, respectively. The existing competitive pollutants such as NOMs or other coexisting ions should be responsible for the loss. Even though the dye degradation efficiencies decreased to a certain degree in water sources containing coexisting pollutants, the relatively high removal rates were all obtained, suggesting that GO/ACR/CN had better pollution capacity and could serve as an efficient photocatalyst in practical application.

### 3.3. Photostability and recyclability

The stability of a photocatalyst is another key issue, in practical applications. The GO/ACR/CN nanocomposite was reused four times in the same process to estimate its photostability. After each cycling test, the catalyst was collected and washed with ethanol and deionized water for three times, then were dried in vacuum at 60 °C for 12 h for the next cycling reused. It could be clearly perceived in Fig. 9A–B that the photocatalytic activity of the GO/ACR/CN nanocomposite had no apparent deactivation even after four successive recycles for the decomposition of RhB or MB under visible light irradiation. Nevertheless, for pure ACR, the degradation efficiencies of RhB (MB) seriously declined from 46.16% (79.52%) to 20.42% (36.30%). The introduction of GO and g-C<sub>3</sub>N<sub>4</sub> was beneficial to solve the photocorrosion of pure ACR to a certain extent, which made the GO/ACR/CN be a stable visible-light photocatalyst for wastewater purification. Three characterization methods (XRD, XPS and FTIR) were employed to further explore the structures changes of pure ACR and GO/ACR/CN sample during cycle experiments. Learning from XRD patterns comparison, a relatively strong peak assigned to metallic Ag at 38.2° appeared in the XRD pattern of pure ACR (Fig. 9C) after four cycles, while no visible peak belonging to metallic Ag was found in the GO/ACR/CN nanocomposite (Fig. 9D). In other words, the higher structural stability of GO/ACR/CN was acquired. The survey spectra and Ag chemical states of ACR and GO/ACR/CN were also investigated and shown in Fig. 10A–D. For pure ACR (Fig. 10C), the peaks located at 366.9 eV and 372.7 eV were ascribed to the binding energies of Ag 3d<sub>3/2</sub> and Ag 3d<sub>5/2</sub> of Ag<sup>+</sup>, whereas the two peaks at 367.5 eV



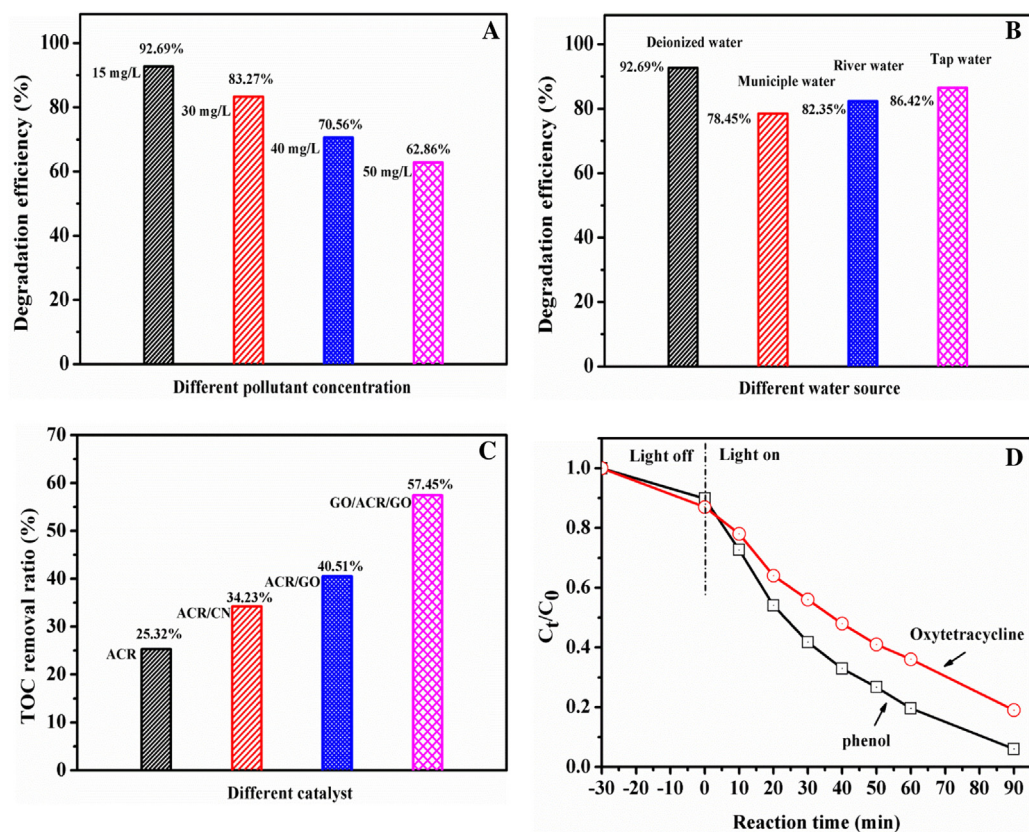


**Fig. 8.** Photocatalytic degradation of MB under different conditions: initial MB concentration (A) and water resources (B), the TOC removal rate over all the prepared samples (C) and other refractory pollutants decomposition with GO/ACR/CN composite (D).

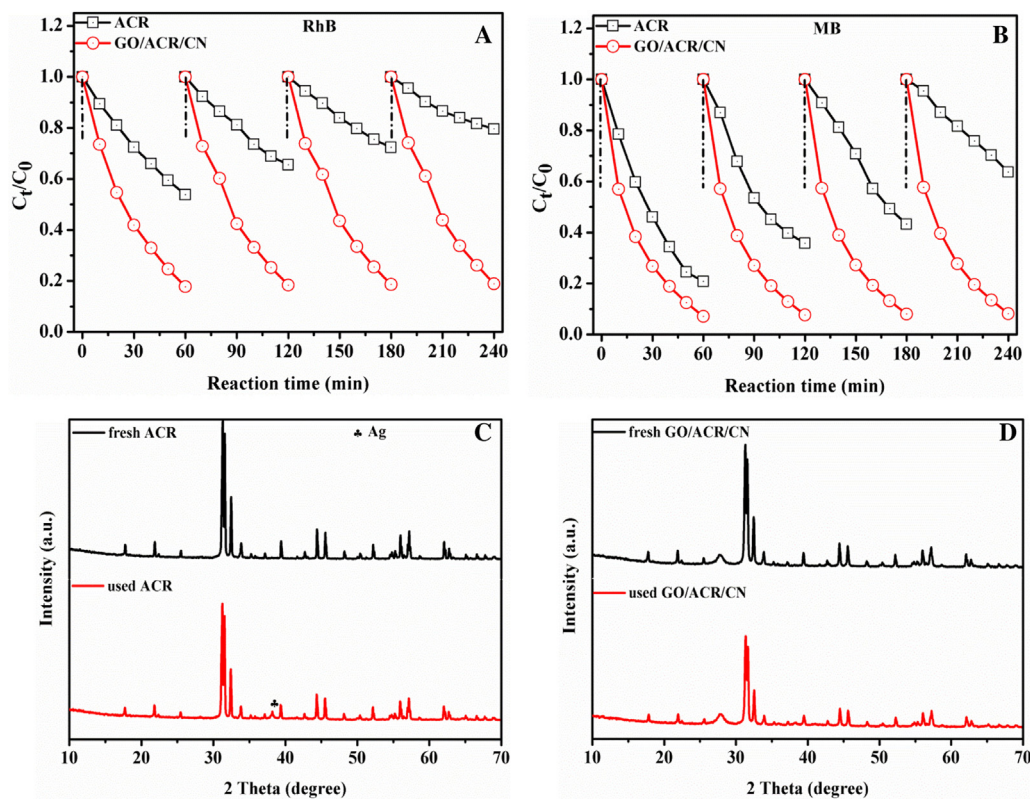


**Fig. 9.** Cycling runs of ACR and GO/ACR/CN for degradation of RhB (A) and MB (B) under visible light irradiation and XRD patterns of the fresh and used ACR (C) and GO/ACR/CN (D).



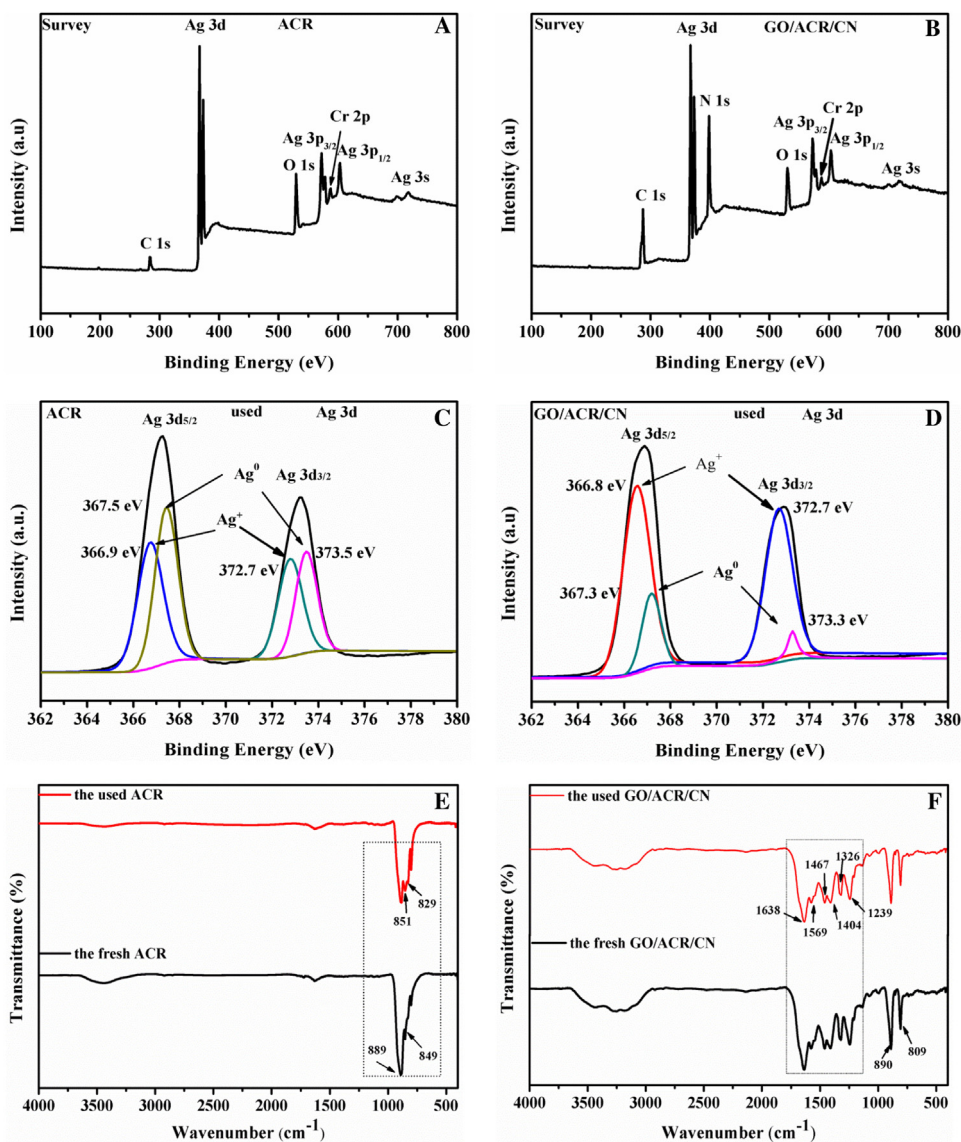


**Fig. 10.** Survey XPS spectra, Ag 3d HRXPS spectra and FTIR spectra of ACR (A, C, E) and GO/ACR/CN (B, D, F) before and after cycling runs.

and 373.5 eV corresponded to the metallic Ag<sup>0</sup>. While for the GO/ACR/CN nanocomposite (Fig. 10D), two peaks at 366.8 eV and 372.7 eV belonged to Ag<sup>+</sup> and the other two peaks at 366.8 eV and 373.3 eV ascribed to Ag<sup>0</sup>. It was clearly displayed that much less metallic Ag was formed in GO/ACR/CN and the photocorrosion of ACR could be effectively inhibited by the introduction of g-C<sub>3</sub>N<sub>4</sub> and GO. Furthermore, the fresh and used FTIR spectra of ACR and GO/ACR/CN were also presented in Fig. 10E–F. The characteristic peak at 889 cm<sup>-1</sup> with a shorter at about 849 cm<sup>-1</sup> in the fresh ACR sample (Fig. 10E) could be assigned to the stretching vibration of the Cr–O bond in CrO<sub>4</sub> tetrahedra [24]. But for the used ACR sample, these two peaks were located 851 cm<sup>-1</sup> and 829 cm<sup>-1</sup>, respectively. The significant translation confirmed that the production of metallic Ag seriously affected the structure of ACR. Compared with the FTIR spectra of the fresh and used GO/ACR/CN, no obvious variations could be observed (Fig. 10F). The peaks at 1638 cm<sup>-1</sup>, 1569 cm<sup>-1</sup>, 1467 cm<sup>-1</sup>, 1404 cm<sup>-1</sup>, 1326 cm<sup>-1</sup> and 1239 cm<sup>-1</sup> were mainly due to the typical stretching vibration modes of CN [32]. Another obvious peak at 809 cm<sup>-1</sup> could be attributable to the characteristic breathing mode of triazine units. The absorption band at 890 cm<sup>-1</sup> was regarded as the characteristic peak of Cr–O in the GO/ACR/CN. The above information indicated that no special changes in the

chemical structure in the GO/ACR/CN, whereas for pure ACR, relatively serious photocorrosion phenomenon was found. That was to say, the presence of CN and GO could effectively improve the photostability and visible-light photoactivity of ACR, which is more advantages in practical applications.

### 3.4. Possible photocatalytic mechanism

The trapping experiments were carried out in order to investigate the main active species in the photocatalytic system and MB was chosen as the target pollutant. From Fig. 11A, it could be found that there was significant decrease of degradation efficiency in the presence of BQ, N<sub>2</sub> purging and EDTA-2Na. Compared with the absence of above quenchers, the removal efficiencies of MB declined from 79.52% to 52.30%, 47.35% and 29.31%, respectively. While for the addition of IPA, no obvious efficiency reduction was observed. The results demonstrated that the •O<sub>2</sub><sup>-</sup> and h<sup>+</sup> should be responsible for ACR photocatalysis. However, the addition of BQ, N<sub>2</sub> purging, IPA and EDTA-2Na could all cause the obvious deactivation to GO/ACR/CN (Fig. 11B), suggesting that •O<sub>2</sub><sup>-</sup>, h<sup>+</sup> and •OH all worked in the degradation process.

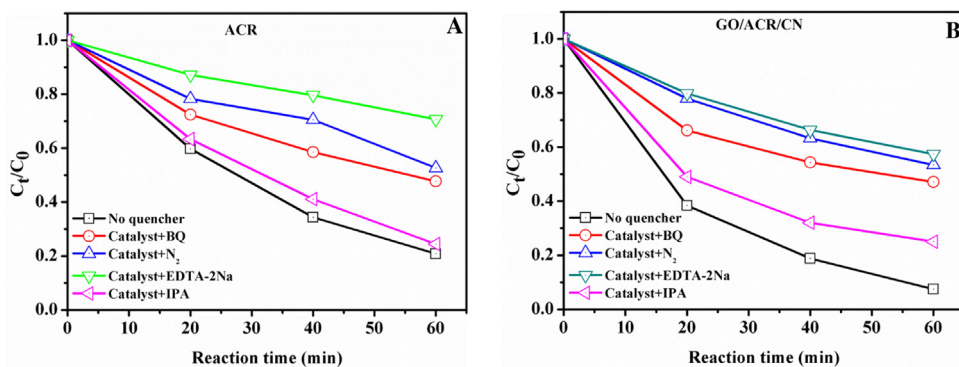


Fig. 11. Effect of different quenchers on the photocatalytic efficiencies of photocatalysts: ACR (A) and GO/ACR/CN (B).

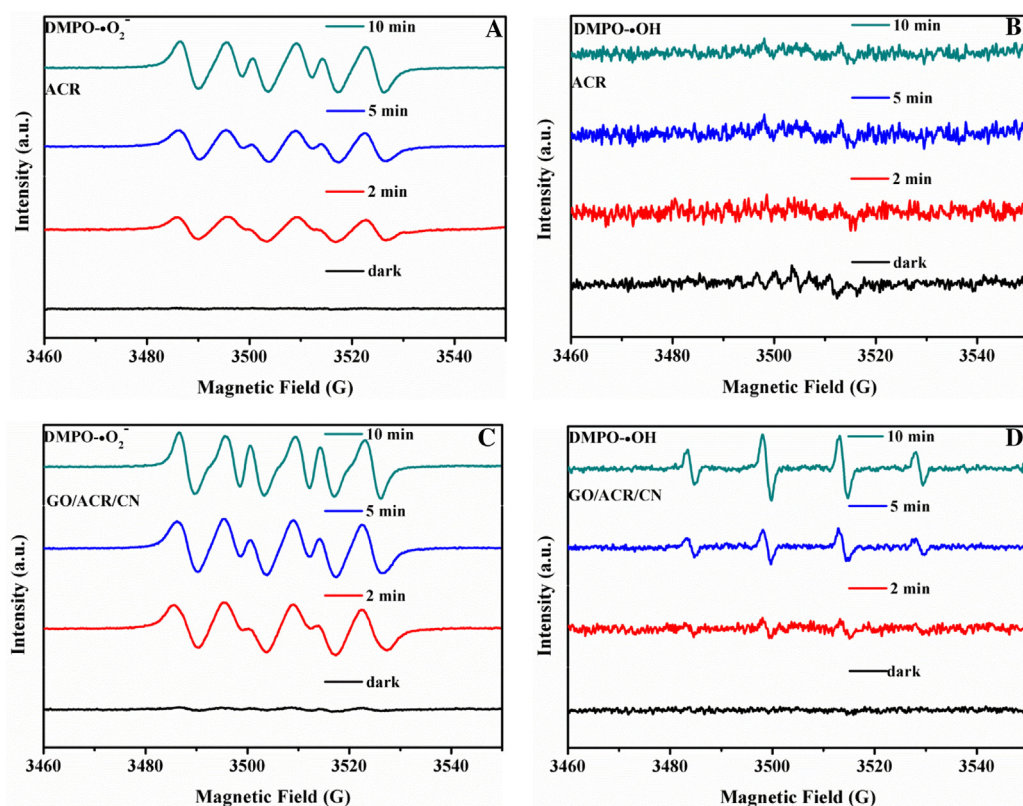


Fig. 12. DMPO spin-trapping ESR spectra for ACR and GO/ACR/CN: (A, C) in aqueous dispersion for DMPO-•O<sub>2</sub><sup>-</sup> and (B, D) in methanol dispersion for DMPO-•OH.

For further confirming the active species, the ESR spin-trap with DMPO technique was also performed (Fig. 12). For both ACR and GO/ACR/CN, no signal of DMPO-•O<sub>2</sub><sup>-</sup> and DMPO-•OH was found in the dark, proving •O<sub>2</sub><sup>-</sup> and •OH radicals were generated during the reaction process. When exposed to visible light irradiation, the signals of •O<sub>2</sub><sup>-</sup> (Fig. 12A and 12C) could be detected for both ACR and GO/ACR/CN, and the corresponding intensities of GO/ACR/CN at given time intervals were higher than that of ACR. The obtained information demonstrated that •O<sub>2</sub><sup>-</sup> radicals were generated in the photodegradation process of pure ACR and GO/ACR/CN, and the amounts of •O<sub>2</sub><sup>-</sup> radicals were bigger in the GO/ACR/CN. Meanwhile, the characteristic peaks of DMPO-•OH couldn't be observed in ACR (Fig. 12B), suggesting no •OH generation during ACR photocatalysis. But for GO/ACR/CN nanocomposite (Fig. 12D), the DMPO-•OH peaks intensity enhanced when the irradiation extended from 2 min to 10 min, indicating that •OH radicals

also formed during the MB degradation. Therefore, the roles of •O<sub>2</sub><sup>-</sup>, h<sup>+</sup> and •OH species were validated in GO/ACR/CN system and only •O<sub>2</sub><sup>-</sup>, h<sup>+</sup> produced in ACR, which was in good accordance with the radicals trapping results.

The transfer and recombination process of electron-hole pairs in the interfaces of nanocomposite photocatalysts is one of the most important factors on the photoactivity [14]. The faster charge carriers transfer and lower photo-generated electrons and holes recombination rate could significantly improve the photocatalytic performance of the catalysts. Photoluminescence (PL) spectrum is widely used to investigate the migration, transfer and recombination of electron-hole pairs. As a result, the PL spectra of the catalysts were collected and presented in Fig. 13. The modified CN and ACR nanocomposites (shown in Fig. 13A–B) exhibited lower PL intensities than pure CN and ACR, respectively. Among all the samples, GO/ACR/CN displayed the lowest PL intensity, implying the efficient



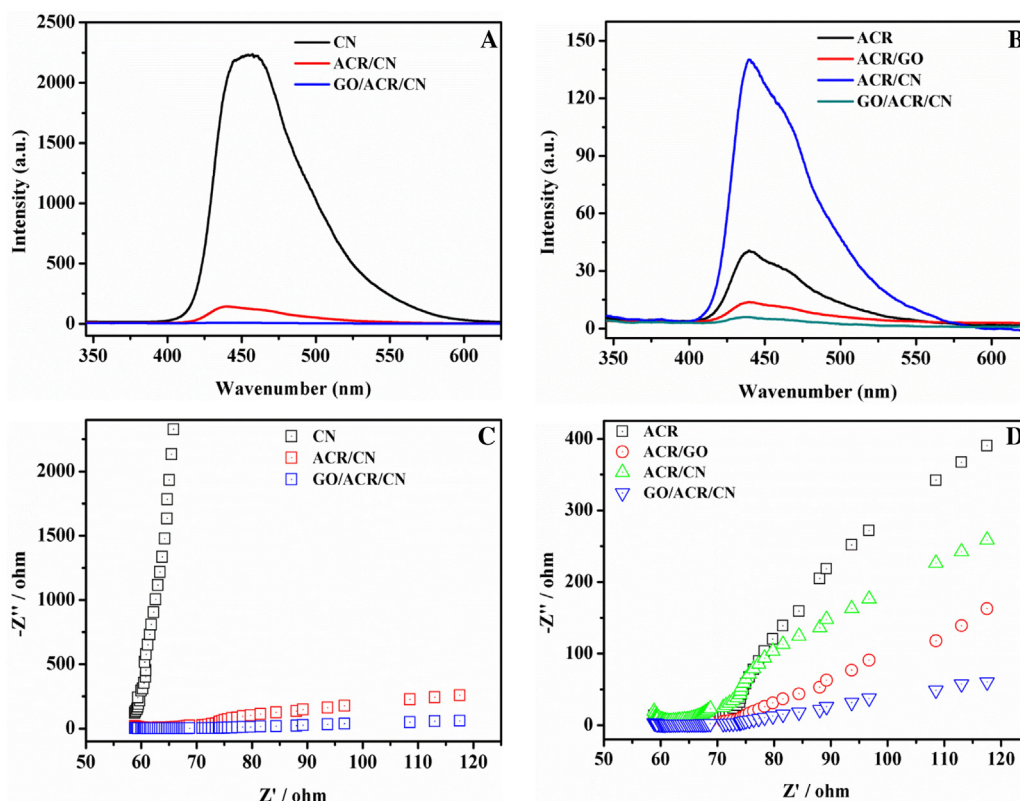


Fig. 13. Photoluminescence spectra (A, B) and electrochemical impedance spectroscopy (EIS) Nyquist plot (C, D) of the prepared samples.

interfacial electron-hole pairs transfer and separation performance, which was favorable for achieving enhanced visible-light photocatalytic activity.

Electrochemical impedance spectra (EIS) also can investigate the charge separation efficiency. The smaller semicircle in the Nyquist plots indicated higher charge carrier transfer efficiency [40]. Fig. 13C–D displayed the EIS spectra of CN- and ACR-based photocatalysts. The modified CN and ACR showed the smaller arc radius under the identical visible-light irradiation, which demonstrated the composite photocatalysts remarkably improved electron-hole pairs separation efficiency. When ACR, GO and CN was simultaneously presented in the catalyst, the smallest radius of curvature on the EIS Nyquist was obtained. The lowest interfacial charge transfer resistance achieving by the GO/ACR/CN suggested the separation and transfer of photo-generated carriers would be accelerated and the photocatalytic activities would be improved. The findings in PL and EIS analysis agree well with results obtained by the photoactivity evaluation.

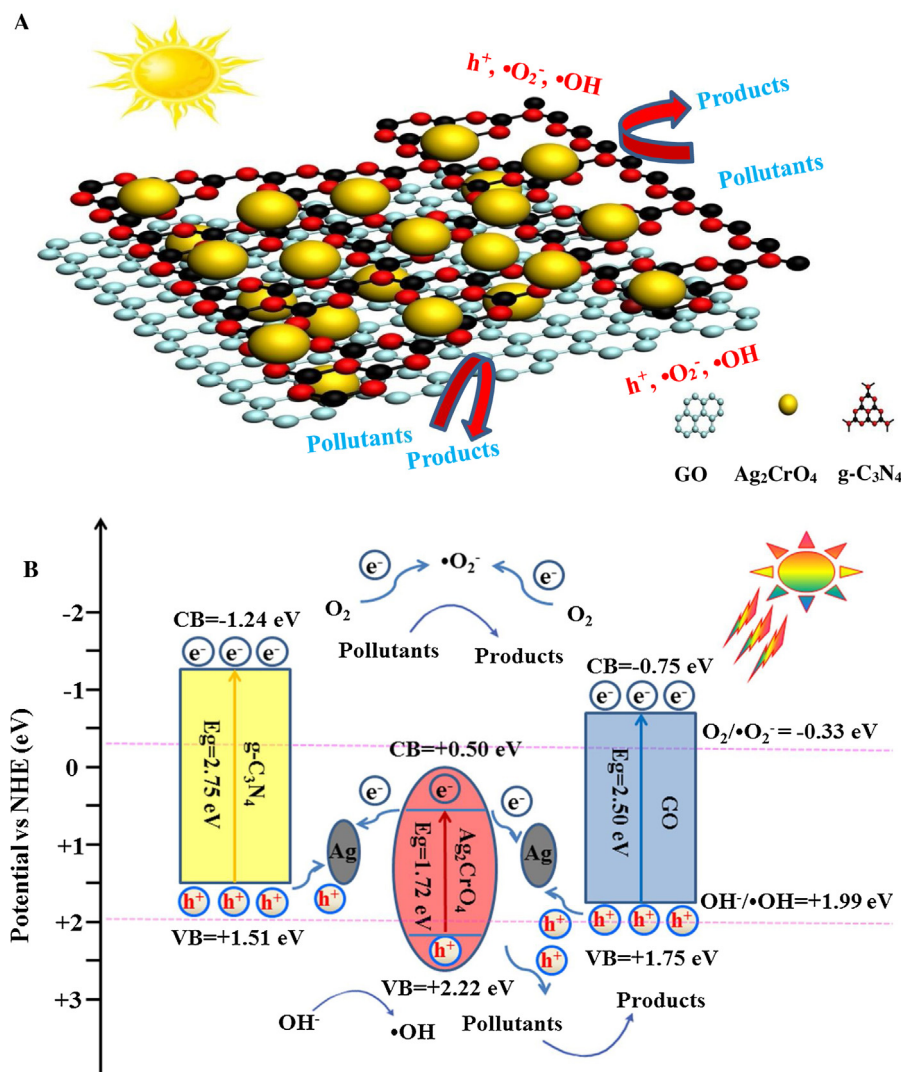
A possible double Z-scheme mechanism for the photodegradation of multiple pollutants using GO/ACR/CN nanocomposite is illustrated in Scheme 1. Under visible light irradiation, ACR, GO and CN could all absorb photons, which excited photo-induced electrons to the conduction band (CB) and simultaneously produced photo-generated holes in the valence band (VB). According to previous reports [24,41], both ACR/GO and ACR/CN binary nanocomposites all fitted well with Z-scheme degradation mechanism. Under the traditional II heterojunction structure, the  $E_{CB}$  (+0.50 eV) of ACR was not negative enough than the  $O_2/\cdot O_2^-$  potential (ca. -0.33 eV [37,42]) and meanwhile the transport of holes from ACR to that of GO or CN was very slow, which couldn't be in good line with the active species results and superior photoactivity achievement. Thus, Z-scheme mechanism was proposed in their studies. Based on the radicals trapping experiments and ESR tests,  $\cdot O_2^-$ ,  $h^+$  and  $\cdot OH$  were all produced in the GO/ACR/CN system. If

the traditional transfer mechanism was adopted, the same problem was also happened in the active species production and photoactivity. So a double Z-scheme mechanism might be possible for the  $\cdot O_2^-$  generation and photocatalytic activity enhancement. As shown in Scheme 1A–B, ACR, GO and CN could all easily excited to generate electrons in the conduction band (CB) and valence band (VB) under visible light irradiation. Due to the CB of ACR is more negative than the Fermi level of metallic Ag, the photogenerated electrons in the CB of ACR would shift to metallic Ag. Simultaneously, the holes in the VB of GO or CN moved to metallic Ag and combined with the electrons. The accumulated holes in the VB of ACR could directly oxidize the pollutants. The electrons left stored in the CB of GO and CN reduced  $O_2$  to yield  $\cdot O_2^-$ , due to the more negative CB of GO (-0.75 eV) and CN (-1.24 eV) than the redox potential of  $O_2/\cdot O_2^-$  (-0.33 eV vs. NHE). A slight amount of produced  $\cdot O_2^-$  and  $H_2O_2$  species were transformed into hydroxyl radicals ( $\cdot OH$ ). Furthermore, the holes in VB of ACR (+2.22 eV vs. NHE) could also oxidize  $OH^-$  to yield  $\cdot OH$  ( $E^0(OH^-/\cdot OH) = +1.99$  eV vs. NHE). Thereby, the forming  $h^+$ ,  $\cdot O_2^-$  and  $\cdot OH$  in the photocatalytic process would react with the pollutants to decompose into smaller molecules or directly transformed into  $CO_2$  and  $H_2O$ . The forming metallic Ag could act as the bridge for accelerating the photo-generated electrons transferring [43,44]. Through this type charge transmission, the separation of photo-induced electron-hole pairs efficiency were efficiently enhanced and the structural stability as well as the photocatalytic activities were also strengthened.

#### 4. Conclusions

In summary, we have successfully fabricated a novel ternary hybrid photocatalyst GO/ACR/CN via a facile chemical precipitation method at ambient conditions. The ternary GO/ACR/CN nanocomposite displayed more superior photocatalytic activity and excellent photostability towards multiple pollutants degrada-





**Scheme 1.** The photocatalytic reaction and charge transfer mechanism of the GO/ACR/CN ternary photocatalyst under visible light irradiation (A, B).

tion. The degradation rate of RhB and MB over GO/ACR/CN ternary nanocomposite was  $0.02849 \text{ min}^{-1}$  and  $0.04329 \text{ min}^{-1}$ , which was 2.73 (5.52) and 1.62 (2.26) folds that of ACR (CN), respectively. The synergistic effect in ternary GO/ACR/CN nanocomposite: effective charge separation, double Z-scheme transfer and enhanced visible-light absorption could be responsible for the improvement of photoactivity. According to active species trapping experiment and ESR measurement,  $\bullet O_2^-$ ,  $h^+$  and  $\bullet OH$  were demonstrated to be the predominant radicals participating in the photodegradation induced by GO/ACR/CN nanocomposite. In addition, the introduction of GO and CN could effectively boost the anti-photocorrosion properties of bare ACR. This work could provide a new approach to construct ternary nanocomposite for the refractory pollutants degradation as well as other environmental remediation applications.

## Acknowledgments

This research was financially supported by the project of National Natural Science Foundation of China (NSFC) (Nos. 51378188, 51478170, 51508178), Doctoral Fund of Ministry of Education of China (20130161120021) and Planned Science and Technology Project of Hunan Province, China (No. 2015SK20672).

## References

- [1] G.M. Zeng, M. Chen, Z.T. Zeng, *Science* 340 (2013) 1403.
- [2] Z.J. Jiang, C.Y. Liu, L.W. Sun, *J. Phys. Chem. B* 109 (5) (2005) 1730–1735.
- [3] A. Houas, H. Lachheb, M. Ksibi, E. Elaloui, C. Guillard, *Appl. Catal. B* 31 (2001) 145–157.
- [4] D.W. Kolpin, E.T. Furlong, M.T. Meyer, *Environ. Sci. Technol.* 36 (2002) 1202–1211.
- [5] F. Chen, Q. Yang, X.M. Li, G.M. Zeng, D.B. Wang, *Appl. Catal. B* 200 (2017) 330–342.
- [6] K. Baransi, Y. Dubowski, I. Sabbah, *Water Res.* 46 (2012) 789–798.
- [7] I. El Saliby, L. Erdei, J.H. Kim, H.K. Shon, *Water Res.* 47 (2013) 4115–4125.
- [8] F. Chen, Q. Yang, Y. Zhong, H.X. An, J.W. Zhao, T. Xie, *Water Res.* 101 (2016) 555–563.
- [9] A. Kudo, Y. Miseki, *Chem. Soc. Rev.* 38 (2009) 253–278.
- [10] Z. Wan, G.K. Zhang, *J. Mater. Chem. A* 3 (2015) 16737–16745.
- [11] S. Kumar, T. Surendar, A. Baruah, V. Shanker, *J. Mater. Chem. A* 1 (2013) 5333–5340.
- [12] H. Wang, X.Z. Yuan, Y. Wu, G.M. Zeng, X.H. Chen, *Appl. Catal. B* 174 (2015) 445–454.
- [13] Y.M. He, L.H. Zhang, B.T. Teng, M.H. Fan, *Environ. Sci. Technol.* 49 (2015) 649–656.
- [14] Z. Zhu, Z.Y. Lu, D.D. Wang, X. Tang, Y.S. Yan, *Appl. Catal. B* 182 (2016) 115–122.
- [15] M. Xu, L. Han, S.J. Dong, *ACS Appl. Mater. Interface* 5 (2013) 12533–12540.
- [16] Y.C. Deng, L. Tang, G.M. Zeng, Z.J. Zhu, M. Yan, *Appl. Catal. B* 203 (2017) 343–354.
- [17] L. Ge, C. Han, J. Liu, *Appl. Catal. A* 409 (2011) 215–222.
- [18] S. Guo, Z. Deng, M. Li, *Angew. Chem. Int. Ed.* 55 (2016) 1830–1834.
- [19] S. Yang, Y. J. Zhang, J. Gong, *Adv. Mater.* 25 (2013) 2452–2456.
- [20] Y.Z. Hong, Y.H. Jiang, C.S. Li, W.Q. Fan, *Appl. Catal. B* 180 (2016) 663–673.
- [21] C.J. Li, S.P. Wang, T. Wang, Y.J. Wei, P. Zhang, *Small* 10 (2014) 2783–2790.

- [22] L.Q. Ye, J.Y. Liu, Z. Jiang, T.Y. Peng, L. Zan, *Appl. Catal. B* 142–143 (2013) 1–7.
- [23] Z. Lu, L. Zeng, W.L. Song, Z.Y. Qin, D.W. Zeng, *Appl. Catal. B* 202 (2017) 489–499.
- [24] Y.Y. Shang, X. Chen, W.W. Liu, P.F. Tan, H.Y. Chen, *Appl. Catal. B* 204 (2017) 78–88.
- [25] Y.C. Deng, L. Tang, G.M. Zeng, J.J. Wang, Y.Y. Zhou, *J. Mol. Catal. A* 421 (2016) 209–221.
- [26] T.T. Li, L.H. Zhao, Y.M. He, J. Cai, M.F. Luo, *Appl. Catal. B* 129 (2013) 255–263.
- [27] F. Chen, Q. Yang, Y.L. Wang, J.W. Zhao, D.B. Wang, *Appl. Catal. B* 205 (2017) 133–147.
- [28] L.Q. Shao, D.L. Jiang, P. Xiao, L.M. Zhu, S.C. Meng, *Appl. Catal. B* 198 (2016) 200–210.
- [29] W.Q. Fan, X.Q. Yu, H.C. Lu, H.Y. Bai, C. Zhang, W.D. Shi, *Appl. Catal. B* 181 (2016) 7–15.
- [30] A.Y. Zhang, W.K. Wang, D.N. Pei, H.Q. Yu, *Water Res.* 92 (2016) 78–86.
- [31] D. Ma, J. Wu, M.C. Gao, Y.J. Xin, T.J. Ma, Y.Y. Sun, *J. Chem. Eng.* 290 (2016) 136–146.
- [32] L.Q. Zhang, X. He, X.W. Xu, C. Liu, Y.L. Duan, L.Q. Hou, *Appl. Catal. B* 203 (2017) 1–8.
- [33] X.L. Yang, F.F. Qian, Y. Wang, M.L. Li, J.R. Lu, *Appl. Catal. B* 200 (2017) 283–296.
- [34] N.N. Wang, Y. Zhou, C.H. Chen, L.Y. Cheng, H.M. Ding, *Catal. Commun.* 73 (2016) 74–79.
- [35] Q. Li, B. Guo, J. Yu, J. Ran, B. Zhang, H. Yan, *J. Am. Chem. Soc.* 133 (2011) 10878–10884.
- [36] T.Y. Liu, B. Liu, L.F. Yang, X.L. Ma, H. Li, S. Yin, *Appl. Catal. B* 204 (2017) 593–601.
- [37] F. Chen, Q. Yang, J. Sun, F.B. Yao, S.N. Wang, *ACS Appl. Mater.* 8 (48) (2016) (20160 32887–32900).
- [38] H. Wang, X.Z. Yuan, Y. Wu, G.M. Zeng, H.R. Dong, *Appl. Catal. B* 186 (2016) 19–29.
- [39] F. Chen, Q. Yang, C.G. Niu, X.M. Li, C. Zhang, *Catal. Commun.* 73 (2016) 1–6.
- [40] A.H. Mady, M.L. Baynosa, D. Tuma, J.J. Shim, *Appl. Catal. B* 203 (2017) 416–427.
- [41] D.F. Xu, B. Cheng, S.W. Cao, J.G. Yu, *Appl. Catal. B* 164 (2015) 380–388.
- [42] D.D. Tang, G.K. Zhang, *Appl. Surf. Sci.* 391 (2017) 415–422.
- [43] D.D. Tang, G.K. Zhang, *Ultrason. Sonochem.* 37 (2017) 208–215.
- [44] T.J. Yan, J. Tian, W.F. Guan, Z. Qiao, W.J. Li, *Appl. Catal. B* 202 (2017) 84–94.